Electronic Supporting Information (ESI) for

Oxygen-promoted catalyst sintering influences number density, alignment, and wall number of vertically aligned carbon nanotubes

Wenbo Shi[a], Jinjing Li[b], Erik S. Polsen[b], C. Ryan Oliver[c], Yikun Zhao[d], Eric R. Meshot[e], Michael Barclay[f], D. Howard Fairbrother[f], A. John Hart[c], Desiree L. Plata[a*]

[a]Department of Chemical and Environmental Engineering, Yale University, New Haven, CT, United States
[b]Department of Mechanical Engineering, University of Michigan, Ann Arbor, MI, United States
[c]Department of Mechanical Engineering and Laboratory for Manufacturing and Productivity, Massachusetts Institute of Technology, Cambridge, MA, United States
[d]Department of Civil and Environmental Engineering, Duke University, Durham, NC, United States
[e]Physical and Life Sciences Directorate, Lawrence Livermore National Laboratory, Livermore, CA, United States
[f]Department of Chemistry, John Hopkins University, Baltimore, MD, United States

*****Corresponding author: desiree.plata@yale.edu; phone: 203-496-3066

Table of Content

Table S1. Summary of the reported beneficial effects of oxygen-containing species on carbon nanomaterials (*i.e.*, CNTs and graphene) synthesis through CVD process

Oxygen-containing Species	Beneficial Effects and Proposed Functioning Mechanisms
H_2O	1) enhance catalyst activity, extend catalyst lifetime, thus increase CNT growth rate and yield;[1-3] 2) etch defects and amorphous carbon in CNTs, therefore improve CNT purity and quality;[1, 4] 3) remove amorphous carbon deposited on catalyst, prevent catalyst poisoning or reactivate catalyst;[5, 6] 4) inhibit catalyst Ostwald ripening, prevent CNT growth termination;[7] 5) enrich semiconducting SWCNTs by *in situ* eteching[8, 9] 6) preferential growth of metallic SWCNTs[10]
O_2	1) balance C and H radical in the gaseous environments to favor SWCNT growth;[11] 2) enhance the capture of $–CH_x$ and enable CNT growth on metal-free catalyst system;[12] 3) remove amorphous carbon, increase SWCNT purity and yield, re-disperse catalyst and generate uniform size of catalyst and as-grown SWCNTs;[13] 4) limit the number of graphene nucleation sites, enable centimeter-scale single-crystal graphene domain growth;[14] 5) increase graphene growth rate by lowering carbon feedstock decomposition energy barrier[15]
CO_2	1) increase CNT purity and yield;[16-18] 2) lower CNT growth temperature;[19-21] 3) enable CNT growth on a broad range of substrates;[20] 4) diminish bulk diffusion of C species, increase catalytic activity, promote feedstock decomposition and yield high quality graphene at a reduced temperature[22]

Using Fe/Al_2O_3 catalyst system, Hata and coworkers[1] developed a water-assisted CVD process to grow single-walled carbon nanotube (SWCNT) forest to 2.5 mm in 10 min with ~150 ppm H_2O addition, overcoming the SWCNTs' limitation of short height and the water was assumed to enhance the catalyst activity and extend its lifetime. However, this super growth procedure ran into difficulties to be repeated in other labs with an identical recipe, exhibiting either optimal H_2O concentration window shift[7, 23-26] or achieving MWCNT instead of SWCNT forest[23, 27-31]. Among the extensive attempts to reproduce super growth, Zhang *et al.*[11] found an alternative way to grow SWCNT arrays by O_2 addition instead of H_2O addition. Although their effects on the growth kinetic features have been recognized and are still debated, the mechanistic role of H_2O and O_2 is still not fully understood. For example, the proposed preventing catalyst poisoning mechanism[5] could be questioned from the controversial functions of catalysts, which on one hand losing activity by coating amorphous carbon and on the other hand catalyzing the ordered C atom structures after receiving carbon atoms[32]

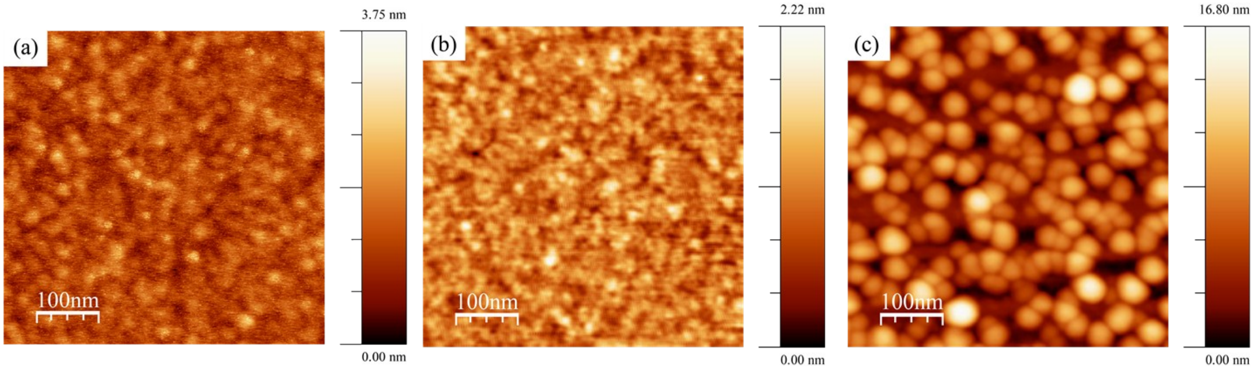

Figure S1. The requirement of H_2 to dewet Fe catalyst thin film. (a) Thin film as-deposited Fe catalyst by e-beam evaporation with a smooth surface (roughness Ra=0.3 nm, analyzed through NanoScope Analysis 1.5). (b) Catalyst annealed in H_2-free (500 sccm Ar) system at 775 ^{o}C for 10 min. Note that the substrate surface (Ra=0.2 nm) is as flat as originally deposited by e-beam evaporation. (c) Catalyst annealed in H_2–rich atmosphere (400 sccm Ar + 100 sccm H_2, 10 min), where dewetting of catalyst nanoparticles is apparent (Ra=2.4 nm). Several other researchers have confirmed this phenomenon implicitly (e.g., Sakurai et al.[33]) or explicitly (e.g., Pisana et al.[34] and Nessim et al.[35]).

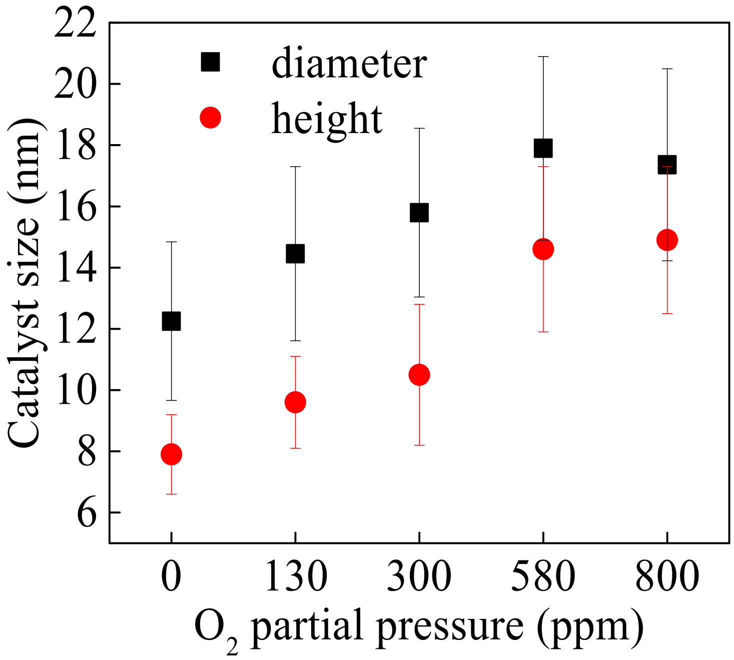

Figure S2. Catalyst diameter and height as a function of O_2 partial pressure. Catalyst nanoparticle diameters closely mirrored the nanoparticle height. Error bars were calculated at least from n=53 measurements for catalyst diameter and at least from n=456 measurement for catalyst height.

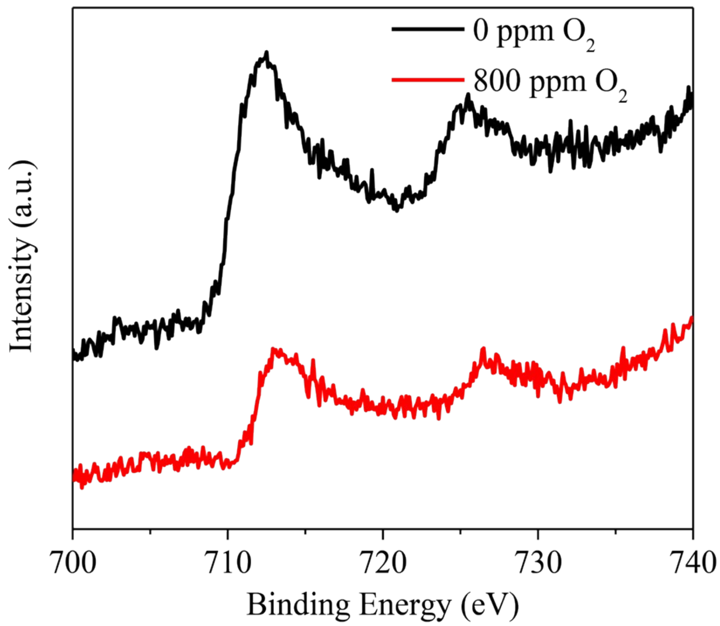

Figure S3. **Comparison of *ex situ* XPS spectrum of Fe (2p) in the extreme morphology difference conditions of our study (*i.e.*, absence (black, top curve) and 800 ppm (red, bottom curve) of O_2 during annealing) exhibited identical chemical composition of those Fe nanoparticles after being exposed to air (*i.e.*, being oxidized to FeOx).** We recognized that FeOx bears larger volume than metallic Fe atom, but note that particle growth at higher O_2 loadings was accompanied by decreased number density, consistent with the migration of smaller particles into larger ones, rather than a change in oxidation state.

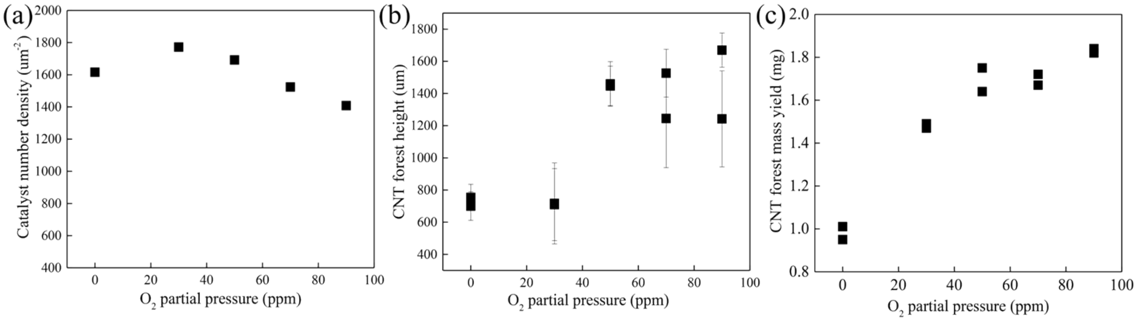

Figure S4. Trace amount of O_2 addition in routine growth recipe (400 sccm He, 100 sccm H_2, and 100 sccm C_2H_4 at 775 °C) didn't substantially impact the catalyst nucleation efficiency. From 0 to 100 ppm O_2, as catalyst particle density decreased slightly (a), the total CNT mass grown on identical substrate size (4 mm by 8 mm) was unchanged (for tubes of similar heights), b and c), suggesting that there was not a significant impact on nucleation efficiency over these O_2 loadings.

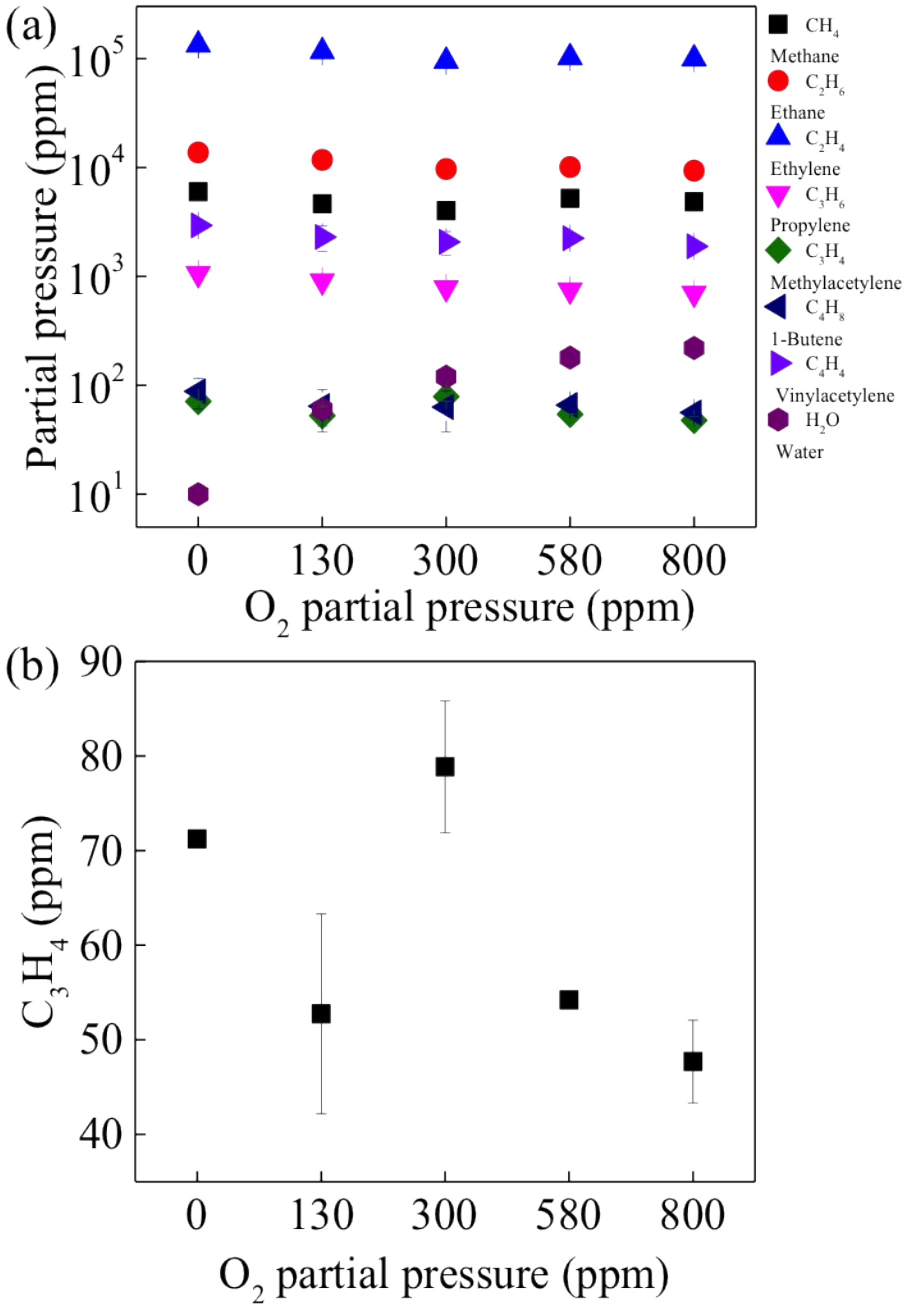

Figure S5. Gas composition analysis showed (a) minor difference for most hydrocarbons along O_2 partial pressure change (b) a local maximum of methyl acetylene concentration at 300 ppm O_2. Gas chromatography with flame ionization detector (GC-FID, HP PLOT-Q column, length 30 m×diameter 0.320 mm×film 20 µm, 60 ^{o}C for 2min, 8 ^{o}Cmin^{-1} to 200 ^{o}C, 2 min hold) was employed to detect the appearance and concentrations of the trace-amount light hydrocarbons with calibration of standard gas mixtures.[36] Water concentrations were measured *in situ* by a hygrometer (Kahn Cermet II).

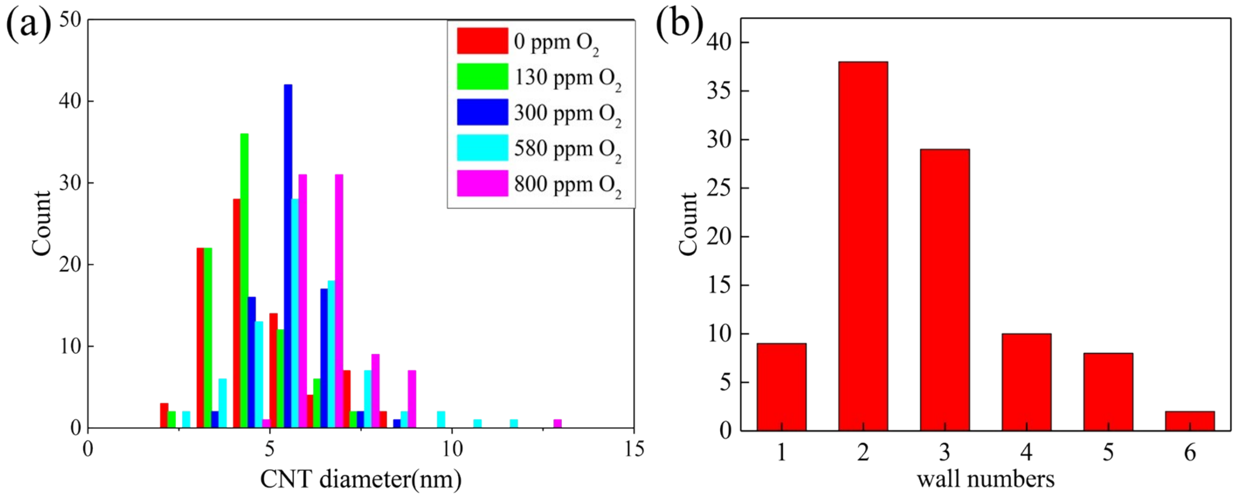

Figure S6. (a) Diameter distribution of CNTs along with O_2 concentration ranging from 0 ppm to 800 ppm and (b) wall number distribution of the CNT sample at 0 ppm O_2 (n=96). Note that for wall number distribution at 0 ppm O_2, where Raman RBM peaks emerged, we only counted isolated tubes (not tubes in bundles) in high-resolution TEM images. This procedural necessity removed a large portion of the sample population from the analytical window and might have artificial biased the image analysis.

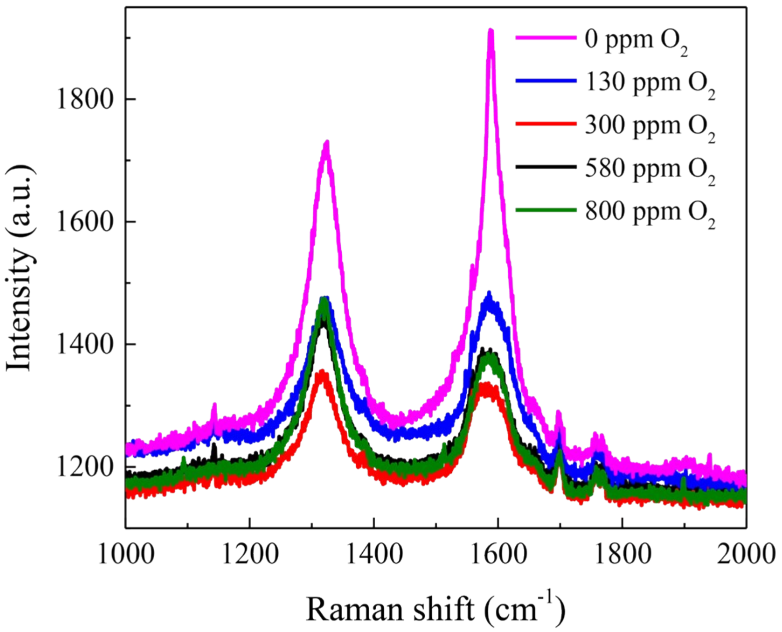

Figure S7. Raman spectra of the CNT forest grown at different O_2 concentration addition (0 ppm to 800 ppm).

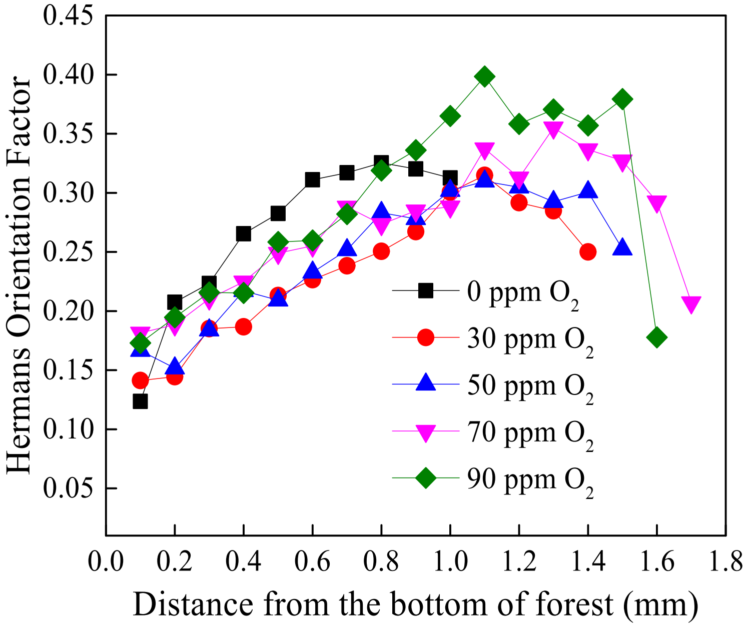

Figure S8. Spatial mapping of HOF within CNT forest grown after 0.8 atm H_2 and below 100 ppm O_2 annealing. The as-grown CNT forest alignment measured by small-angle x-ray scattering (SAXS) didn't vary systematically in the confined region below 100 ppm O_2. A different HOF fitting exercise was conducted here[37, 38], where the two algorithms tend to give a different range of values. Thus, the results can be compared within an analytical method set, but not between sets (*e.g.*, image analysis and SAXS analysis numbers can not be compared directly).

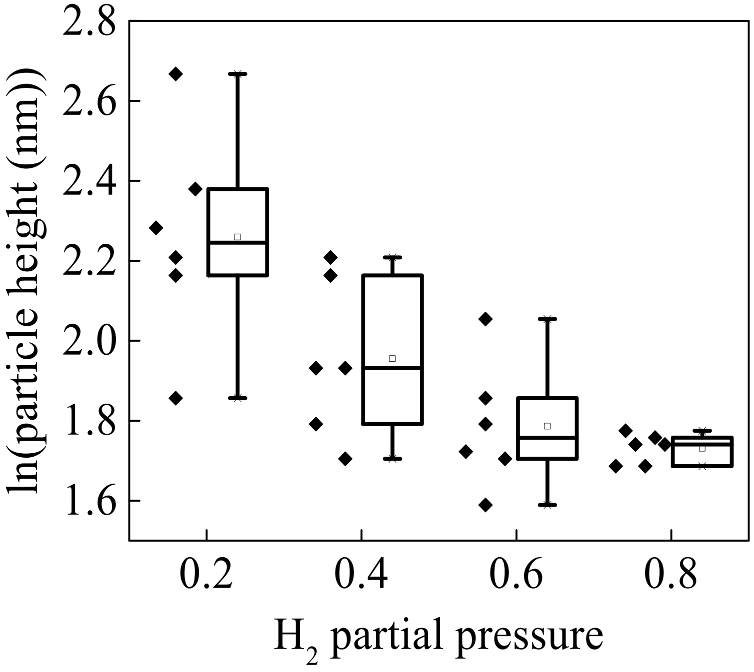

Figure S9. Average particle height of the 0-100 ppm O_2 study grouped by H_2 partial pressure. Anova analysis returned a significant difference between the four groups ($p<0.05$).

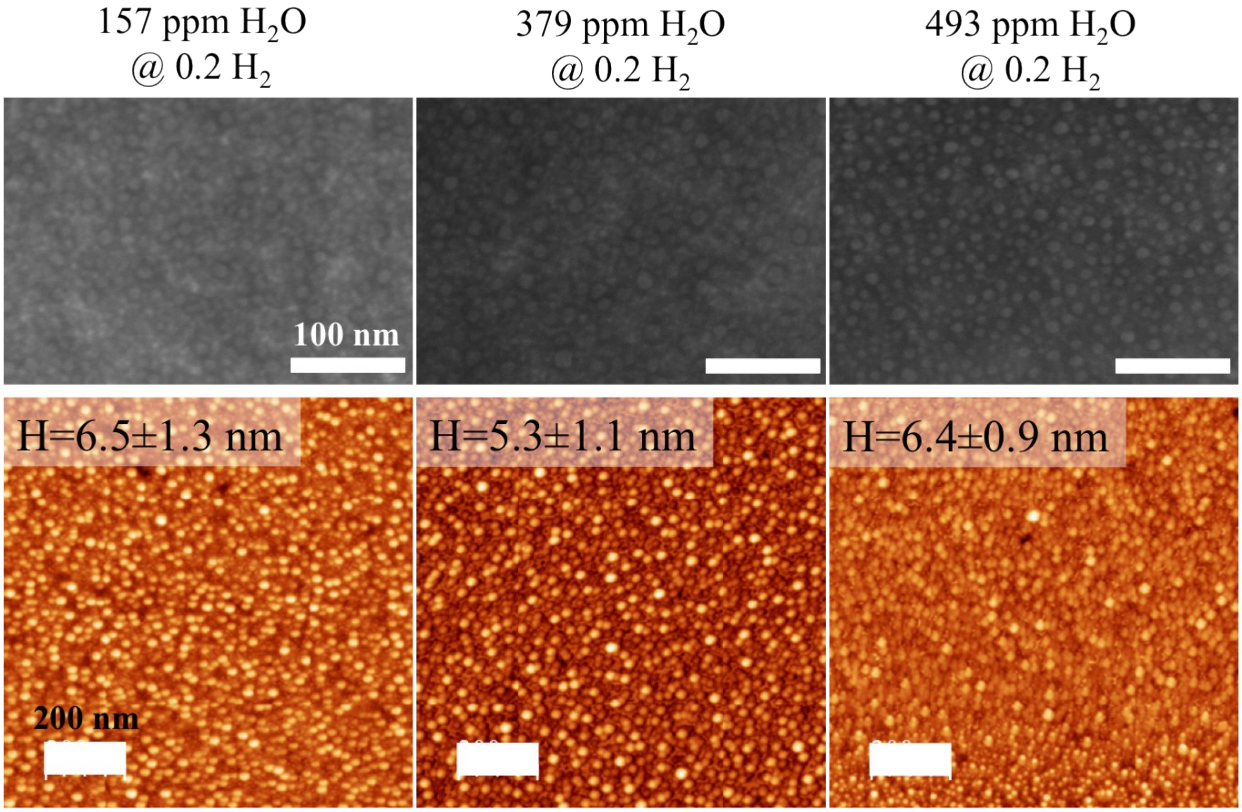

Figure S10. SEM and AFM images of the Fe catalyst annealed at 0.2 H_2 partial pressure with varied moisture levels in an O_2-free system (*i.e.*, a water bubbler was used for H_2O vapor delivery and moisture level was measured with a hygrometer). Average particle height (H) was labeled for each AFM image. Error bars were calculated from at least n=2159 particles.

Moisture in a reactor can come from several sources: (1) all gas canisters carry a certain amount of moisture, (2) moisture is adsorbed onto reactor equipment and gas delivery lines, and (3) O_2 and other oxygen-containing moieties will react with H_2 and increase the moisture level inside the reactor. To demonstrate that the observed phenomenon resulted from O_2 instead of H_2O, we utilized water bubbler to intentionally deliver H_2O into the reactor and annealed the catalyst at 0.2 H_2 partial pressure. In contrast to Ostwald-ripening suppressing effect of H_2O reported by Amama *et al.*[7] (comparing 0.5% H_2O with H_2O-free) the particle sizes annealing in the moisture range from 150 ppm to 500 ppm were identical, suggesting H_2O has no effect on catalyst coarsen, consistent with reports from Hasegawa *et al*.[24] and Zhong *et al*.[39]

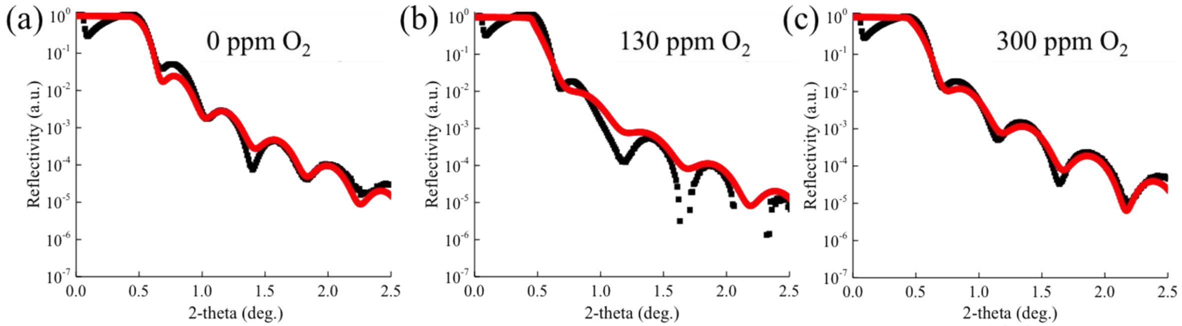

Al_2O_3
Thickness 20.2 nm
Density 3.2 g/cm^3

Al_2O_3
Thickness 16.7 nm
Density 2.8 g/cm^3

Al_2O_3
Thickness 16.8 nm
Density 3.0 g/cm^3

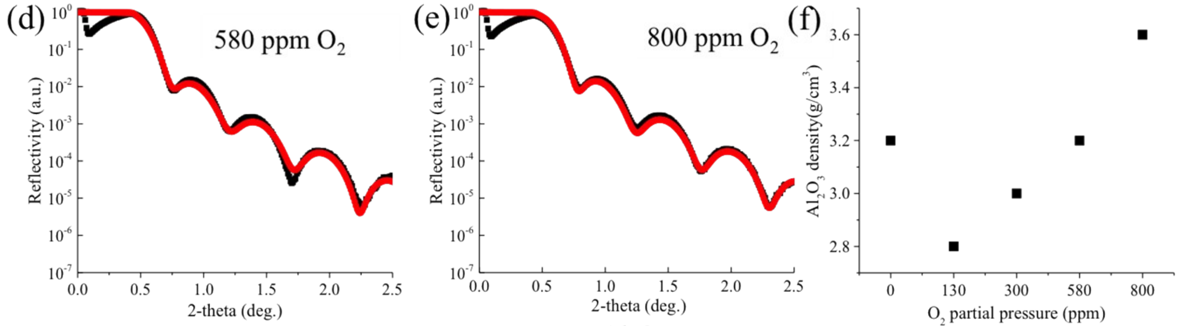

Al_2O_3
Thickness 16.2 nm
Density 3.2 g/cm^3

Al_2O_3
Thickness 15.8 nm
Density 3.6 g/cm^3

Figure S11. X-ray reflectivity (XRR) curves of annealed Al_2O_3-supported Fe catalysts at 0 to 800 ppm O_2. Original data points appear in black and fitted lines appear in red (a-e). The calculated Al_2O_3 layer thickness and density are present below each curve and summarized in f.

XRD patterns were consistent with amorphous Al_2O_3 and fitting data from XRR showed a modest increase in Al_2O_3 density with increasing O_2 partial pressure (except for the 0 ppm O_2 case), from 2.8 to 3.6 g/cm^3, which is the range of reported 2.1-3.6 g/cm.[3, 40, 41] While aluminum itself can take on only a single oxidation state, the network of amorphous alumina may exhibit oxygen deficiencies as the ambient oxygen level decreases. Such a deficiency could manifest as decreased density in the alumina, as observed. Note that the thickness of the alumina layer did not undergo a significant commensurate change (*i.e.*, one that could explain the loss of density in the alumina layer as oxygen decreased). Unfortunately, error estimates are not available from the standard XRR fitting routines (GlobalFit, Rigaku).

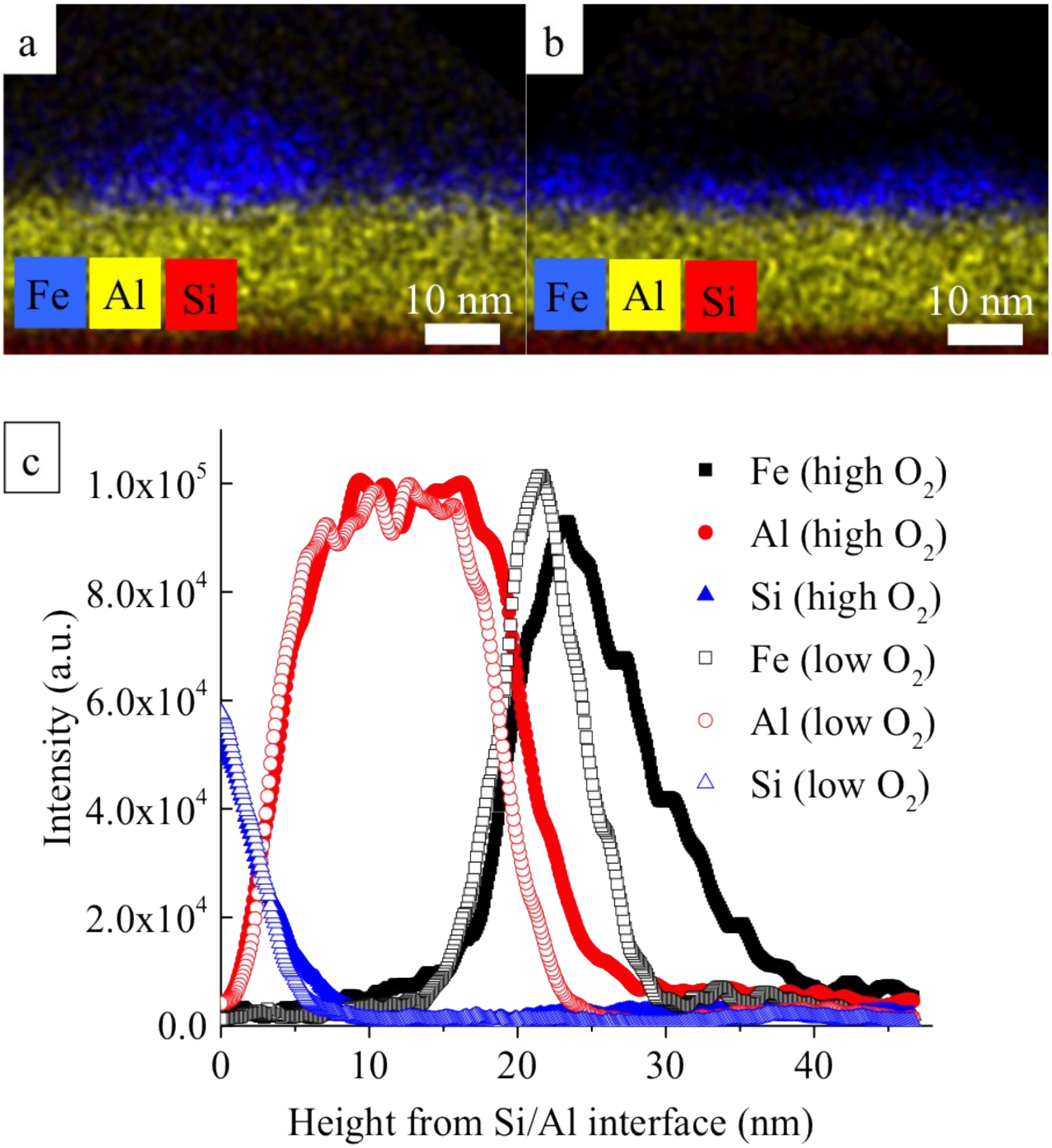

Figure S12. Zoomed-in cross-sectional Scanning Transmission Electron Microscope (STEM) images of the Fe-Al_2O_3-Si interface at (a) O_2-abundant and (b) O_2-scarce annealing conditions. (c) The element depth profile derived from Energy Dispersive X-ray (EDX) mapping demonstrated no subsurface diffusion occurred in either case. The intensity of each element at certain height was calculated by summing up the intensity of each corresponding color along horizontal pixels. Note that the ordinate marks the depth of the Si/Al interface, and increasing numbers approach the surface of the substrate (as pictured in (a) and (b)). The broad shape of the solid black squares (Fe in the high O_2 case) are a result of the particle height rather than element mobility, spreading, or mixing. Also note that the relative intensity of the Fe and Al signals at the Fe/Al interface is nearly identical in both the O_2-rich and O_2-free condition.

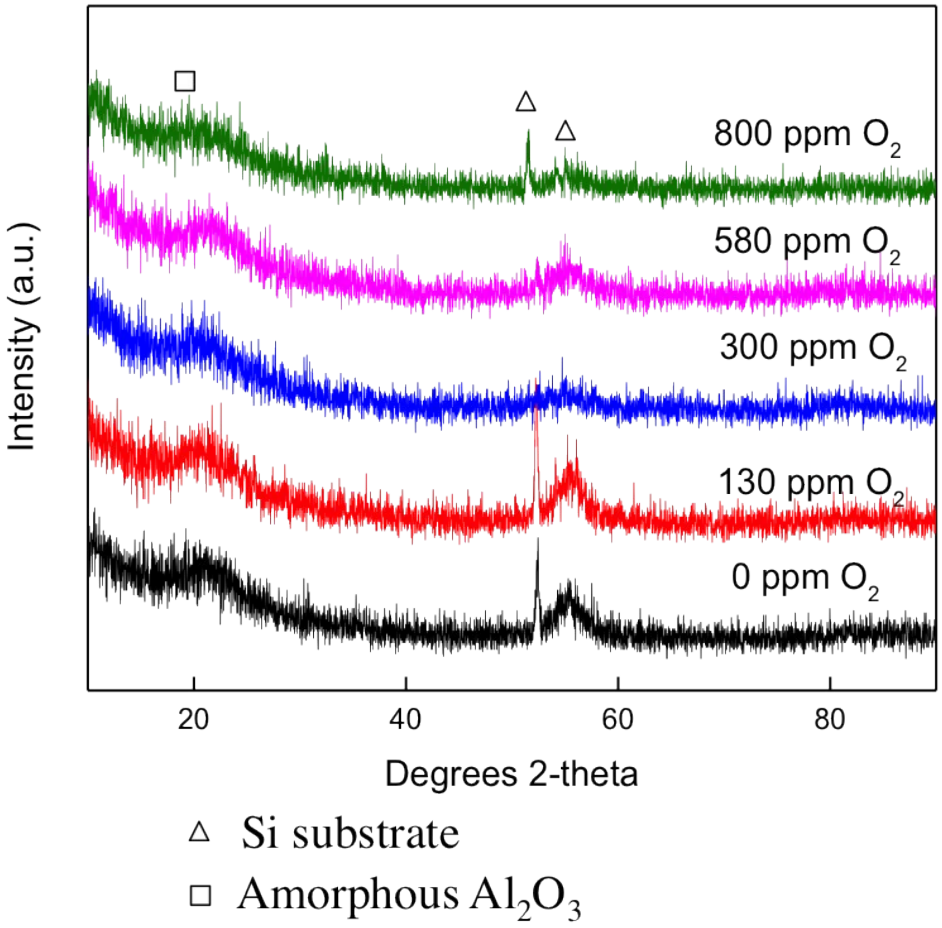

Figure S13. Thin film X-ray diffraction (XRD) pattern of the annealed Al_2O_3-supported Fe catalysts from 0 to 800 ppm O_2 demonstrating that Al_2O_3 was in amorphous phase. Crystalline Al_2O_3 would present multiple apparently sharp peaks at different 2-theta positions.[42]

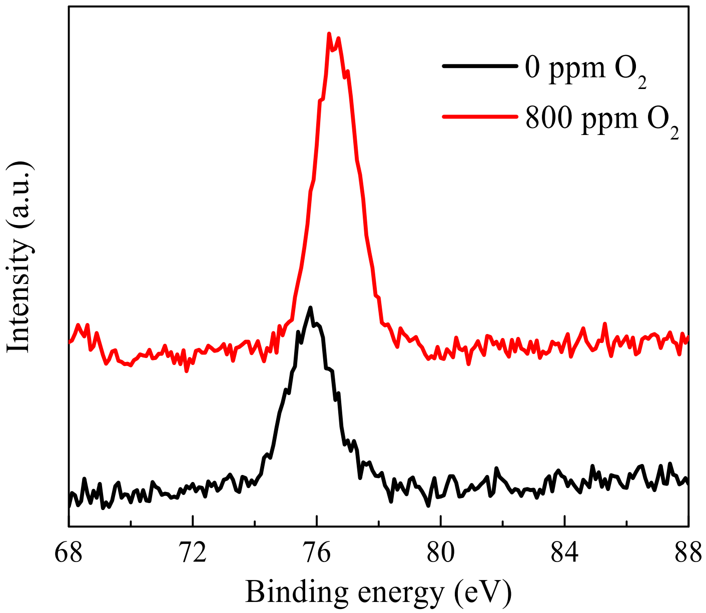

Figure S14. Binding energy shift of Al (2p) in the presence (red, top curve) and absence (black, bottom curve) of O_2 during annealing.

From the X-ray photoelectron spectroscopy (XPS) spectra, we isolated the Al (2p) region on the surface and found that the Al (2p) experienced a slight upshift under O_2 during annealing, which might indicate that the Al (2p) was in a slightly higher energy valence status[43] under O_2 due to the variation of Al-O coordination in amorphous Al_2O_3.

References

1. K. Hata, D. N. Futaba, K. Mizuno, T. Namai, M. Yumura and S. Iijima, *Science*, 2004, **306**, 1362-1364.
2. D. N. Futaba, K. Hata, T. Yamada, K. Mizuno, M. Yumura and S. Iijima, *Phys. Rev. Lett.*, 2005, **95**.
3. D. N. Futaba, K. Hata, T. Namai, T. Yamada, K. Mizuno, Y. Hayamizu, M. Yumura and S. Iijima, *J. Phys. Chem. B*, 2006, **110**, 8035-8038.
4. T. Yamada, T. Namai, K. Hata, D. N. Futaba, K. Mizuno, J. Fan, M. Yudasaka, M. Yumura and S. Iijima, *Nat. Nanotechnol.*, 2006, **1**, 131-136.
5. T. Yamada, A. Maigne, M. Yudasaka, K. Mizuno, D. N. Futaba, M. Yumura, S. Iijima and K. Hata, *Nano Lett.*, 2008, **8**, 4288-4292.
6. N. Yoshihara, H. Ago and M. Tsuji, *J. Phys. Chem. C*, 2007, **111**, 11577-11582.
7. P. B. Amama, C. L. Pint, L. McJilton, S. M. Kim, E. A. Stach, P. T. Murray, R. H. Hauge and B. Maruyama, *Nano Lett.*, 2009, **9**, 44-49.
8. P. Li and J. Zhang, *J. Mater. Chem.*, 2011, **21**, 11815-11821.
9. W. W. Zhou, S. T. Zhan, L. Ding and J. Liu, *J. Am. Chem. Soc.*, 2012, **134**, 14019-14026.
10. A. R. Harutyunyan, G. G. Chen, T. M. Paronyan, E. M. Pigos, O. A. Kuznetsov, K. Hewaparakrama, S. M. Kim, D. Zakharov, E. A. Stach and G. U. Sumanasekera, *Science*, 2009, **326**, 116-120.
11. G. Y. Zhang, D. Mann, L. Zhang, A. Javey, Y. M. Li, E. Yenilmez, Q. Wang, J. P. McVittie, Y. Nishi, J. Gibbons and H. J. Dai, *P. Natl. Acad. Sci. USA*, 2005, **102**, 16141-16145.
12. B. L. Liu, D. M. Tang, C. H. Sun, C. Liu, W. C. Ren, F. Li, W. J. Yu, L. C. Yin, L. L. Zhang, C. B. Jiang and H. M. Cheng, *J. Am. Chem. Soc.*, 2011, **133**, 197-199.
13. Q. Wen, W. Z. Qian, F. Wei and G. Q. Ning, *Nanotechnology*, 2007, **18**, 215610.
14. Y. F. Hao, M. S. Bharathi, L. Wang, Y. Y. Liu, H. Chen, S. Nie, X. H. Wang, H. Chou, C. Tan, B. Fallahazad, H. Ramanarayan, C. W. Magnuson, E. Tutuc, B. I. Yakobson, K. F. McCarty, Y. W. Zhang, P. Kim, J. Hone, L. Colombo and R. S. Ruoff, *Science*, 2013, **342**, 720-723.
15. X. Xu, Z. Zhang, L. Qiu, J. Zhuang, L. Zhang, H. Wang, C. Liao, H. Song, R. Qiao, P. Gao, Z. Hu, L. Liao, Z. Liao, D. Yu, E. Wang, F. Ding, H. Peng and K. Liu, *Nat. Nanotechnol.*, 2016, **11**, 930-935.
16. A. Magrez, J. W. Seo, V. L. Kuznetsov and L. Forro, *Angew. Chem. Int. Ed. Engl.*, 2007, **46**, 441-444.
17. Q. Wen, W. Z. Qian, F. Wei, Y. Liu, G. Q. Ning and Q. Zhang, *Chem. Mater.*, 2007, **19**, 1226-1230.
18. Z. R. Li, Y. Xu, X. D. Ma, E. Dervishi, V. Saini, A. R. Biris, D. Lupu and A. S. Biris, *Chem. Commun.*, 2008, DOI: Doi 10.1039/B803465f, 3260-3262.
19. A. G. Nasibulin, D. P. Brown, P. Queipo, D. Gonzalez, H. Jiang and E. I. Kauppinen, *Chem. Phys. Lett.*, 2006, **417**, 179-184.

20. A. Magrez, J. W. Seo, R. Smajda, B. Korbely, J. C. Andresen, M. Mionic, S. Casimirius and L. Forro, *ACS Nano*, 2010, **4**, 3702-3708.
21. A. Magrez, J. W. Seo, R. Smajda, M. Mionic and L. Forro, *Materials*, 2010, **3**, 4871-4891.
22. I. H. Son, H. J. Song, S. Kwon, A. Bachmatiuk, S. J. Lee, A. Benayad, J. H. Park, J. Y. Choi, H. Chang and M. H. Rummeli, *ACS Nano*, 2014, **8**, 9224-9232.
23. M. Stadermann, S. P. Sherlock, J. B. In, F. Fornasiero, H. G. Park, A. B. Artyukhin, Y. M. Wang, J. J. De Yoreo, C. P. Grigoropoulos, O. Bakajin, A. A. Chernov and A. Noy, *Nano Lett.*, 2009, **9**, 738-744.
24. K. Hasegawa and S. Noda, *ACS Nano*, 2011, **5**, 975-984.
25. J. B. In, C. P. Grigoropoulos, A. A. Chernov and A. Noy, *Appl. Phys. Lett.*, 2011, **98**.
26. R. M. Wyss, J. E. Klare, H. G. Park, A. Noy, O. Bakajin and V. Lulevich, *ACS Appl. Mater. Interface*, 2014, **6**, 21019-21025.
27. G. D. Nessim, A. Al-Obeidi, H. Grisaru, E. S. Polsen, C. R. Oliver, T. Zimrin, A. J. Hart, D. Aurbach and C. V. Thompson, *Carbon*, 2012, **50**, 4002-4009.
28. C. R. Oliver, E. S. Polsen, E. R. Meshot, S. Tawfick, S. J. Park, M. Bedewy and A. J. Hart, *ACS Nano*, 2013, **7**, 3565-3580.
29. J. J. Li, M. Bedewy, A. O. White, E. S. Polsen, S. Tawfick and A. J. Hart, *J. Phys. Chem. C*, 2016, **120**, 11277-11287.
30. Y. H. Yun, V. Shanov, Y. Tu, S. Subramaniam and M. J. Schulz, *J. Phys. Chem. B*, 2006, **110**, 23920-23925.
31. W. D. Cho, M. Schulz and V. Shanov, *Carbon*, 2014, **69**, 609-620.
32. P. T. A. Reilly and W. B. Whitten, *Carbon*, 2006, **44**, 1653-1660.
33. S. Sakurai, M. Inaguma, D. N. Futaba, M. Yumura and K. Hata, *Small*, 2013, **9**, 3584-3592.
34. S. Pisana, M. Cantoro, A. Parvez, S. Hofmann, A. C. Ferrari and J. Robertson, *Phys. E*, 2007, **37**, 1-5.
35. G. D. Nessim, A. J. Hart, J. S. Kim, D. Acquaviva, J. H. Oh, C. D. Morgan, M. Seita, J. S. Leib and C. V. Thompson, *Nano Lett.*, 2008, **8**, 3587-3593.
36. D. L. Plata, A. J. Hart, C. M. Reddy and P. M. Gschwend, *Environ. Sci. Technol.*, 2009, **43**, 8367-8373.
37. E. R. Meshot and A. J. Hart, *Appl. Phys. Lett.*, 2008, **92**.
38. M. Bedewy, E. R. Meshot, M. J. Reinker and A. J. Hart, *ACS Nano*, 2011, **5**, 8974-8989.
39. G. Zhong, S. Hofmann, F. Yan, H. Telg, J. H. Warner, D. Eder, C. Thomsen, W. I. Milne and J. Robertson, *J. Phys. Chem. C*, 2009, **113**, 17321-17325.
40. K. Koski, J. Holsa and P. Juliet, *Thin Solid Films*, 1999, **339**, 240-248.
41. C. Arhammar, A. Pietzsch, N. Bock, E. Holmstrom, C. M. Araujo, J. Grasjo, S. X. Zhao, S. Green, T. Peery, F. Hennies, S. Amerioun, A. Fohlisch, J. Schlappa, T. Schmitt, V. N. Strocov, G. A. Niklasson, D. C. Wallace, J. E. Rubensson, B. Johansson and R. Ahuja, *P. Natl. Acad. Sci. USA*, 2011, **108**, 6355-6360.
42. S. Cava, S. M. Tebcherani, I. A. Souza, S. A. Pianaro, C. A. Paskocimas, E. Longo and J. A. Varela, *Mater. Chem. Phys.*, 2007, **103**, 394-399.
43. S. Hofmann, *Auger- and X-ray Photoelectron Spectroscopy in Materials Science : A User-Oriented Guide*, Springer:Germany, 2013.